Chapter 4

Sol-gel synthesized Co-doped Ilmenite-$NiTiO_3$ for Oxygen Evolution Reaction: Interplay of Inductive Effect and Crystal Structure

4.1 Introduction

The excessive utilization of carbon-based fossil fuels has shown a detrimental effect on the environment. Therefore, the researchers are driven to discover alternative, environment-friendly, and sustainable energy systems to fulfill the need for energy. [1] Several innovative ideas and strategies have been created to achieve efficient and environment-friendly alternative/renewable energy conversion and storage systems such as supercapacitors, batteries, photocatalysis and electrocatalysis. [2-5] Water electrolysis is a green and clean approach for the production of H_2 and O_2. Overall electrochemical water splitting is a promising energy conversion method that incorporates two half-reactions: the hydrogen evolution reaction (HER) at the cathode and the oxygen evolution reaction (OER) at the anode. However, OER is slower than HER because it takes four electrons for the reaction, while HER only needs two electrons. Thus, the OER is crucial for the overall effectiveness of electrocatalytic water splitting. [6]

$$2H_2O \rightarrow O_2 + 4H^+ + 4e^- \quad (4.1)$$

The OER and oxygen reduction reaction (ORR) are crucial electrochemical processes that significantly impact the efficiency of fuel cells and metal-air batteries. [7] Although some noble metals and their corresponding compounds, such as Pt, RuO_2 and IrO_2 demonstrate significant catalytic activity for ORR or OER, however their extensive utilization or large-scale use is hindered by their high cost and limited availability. [8, 9]

Many efforts have been made to substitute benchmark catalysts with transition metal-based materials for the OER. Among these alternatives, nickel-based catalysts have shown promising catalytic activity for OER in alkaline environments. [10] The strategic design of nickel oxide-based materials provides a reliable approach to utilize the synergistic interactions among the constituent materials, aiding in addressing the challenges associated with oxygen electrocatalysis. [11] Consequently, a wide variety of transition-metal

compounds, including transition-metal oxides (e.g., Mn, Fe, Co, and Ni), (oxy)hydroxides, chalcogenides, carbides, phosphides, nitrides and their related composite electrocatalysts, have been synthesized. [12] The advancement of oxygen evolution catalysts (OECs) for electrocatalytic methods, which has seemingly received more attention, has resulted in the emergence of several widely recognized Co- and Ni-based materials. [13] Most investigations into the OER primarily focus on perovskite and spinel-type oxides, however, there has been limited exploration of other nickel-based mixed metal oxides specifically ABO_3 type ilmenites. [14]

The synthesized $NiTiO_3$ exhibits an ilmenite-type structure characterized by octahedral coordination of both nickel and titanium cations. In this arrangement, the cation layers are alternately occupied by Ni^{2+} and Ti^{4+} ions, while both the corundum and ilmenite structures display six-fold coordination with oxygen. The coordination number and arrangement of cations in $NiTiO_3$ play a significant role in shaping their electronic, magnetic and catalytic properties, which in turn influences their potential applications in advanced technologies. [15]

In line with this methodology, several types of ABO_3 perovskites have been evaluated for their electrocatalytic activity in the oxygen evolution reaction. [16, 17] Various formations including earth-abundant elements in the transition metal position (B), such as $LaNiO_3$ and $LaCoO_3$, exhibited an activity trend outlined as Ni > Co > Fe > Mn > Cr. These results emphasized the exceptional catalytic efficiency of Ni and Co, which has also been demonstrated in recent investigations including various materials with structures resembling $BaNiO_3$ like $Ba_{0.5}Sr_{0.5}Co_{0.8}Fe_{0.2}O_3$. [17]

Some researchers have found that the combination of Ni and Co into $Ni_xCo_{3-x}O_4$ [18-20] systems exhibits enhanced activity for oxygen evolution reaction. Similarly, many nickel

and cobalt incorporated hetero-structures such as ultrafine NiO nanosheets supported by TiO_2, [21] cobalt-doped black TiO_2 nanotube arrays, [22] polymorph-$NiTiO_3$, [23] $NiTiO_3$/Ni, [24] are of particular relevance for OER in basic media.

Following this strategy and motivated by the high performances of Ni, Co-based materials as OER catalysts, In the present work, we describe the successful synthesis of Co-doped $NiTiO_3$ ilmenite structure via sol-gel method and evaluate it as an electrocatalyst for OER. Ni, Ti, and Co have their distinct oxidation states (4+ for Ti, 2+ for Ni, and 2+/3+ for Co) and are present in the same crystal structure in the composition $Ni_{1-x}Co_xTiO_3$ ($0 \leq x \leq 0.25$). The incorporation of foreign metal substituents to adjust the redox potential has been demonstrated as a very efficient approach to enhance the efficiency of oxygen electrocatalysis. [25] The inductive effect, resulting from differences in electronegativity, is commonly observed in multicomponent materials. More electronegative substitutes or components tend to draw the electron cloud of chemical bonds, which provides the tuned surface electronic structure of the catalyst. [26]

The presence of Co^{3+} at the Ni site within the ilmenite lattice $Ni_{1-x}Co_xTiO_3$ induces an inductive effect that enhances the OER activity. From linear sweep voltammograms (LSV) results, we found that cobalt doping in $Ni_{1-x}Co_xTiO_3$ ($0 \leq x \leq 0.25$) increases the OER activity and the best OER activity is achieved for $Ni_{0.825}Co_{0.175}TiO_3$ with a Tafel slope of 56 mV dec^{-1} and an overpotential of 395 mV at a current density of 10 mA cm^{-2}.

4.2 Experimental Section

4.2.1 Material Synthesis

A sol-gel synthesis route was utilized to synthesize polycrystalline $Ni_{1-x}Co_xTiO_3$ (x = 0, 0.05, 0.1, 0.15, 0.175, 0.2, 0.25) powder sample. Stoichiometric quantity of precursor compounds such as $Ni(CH_3COO)_2.6H_2O$ (Sigma Aldrich, ≥ 99 %), $Co(CH_3COO)_2.6H_2O$ (Sigma Aldrich,

≥ 99 %) $(C_3H_7O)_4Ti$, titanium isopropoxide (TIP) (Sigma Aldrich, ≥ 98 %), were used as received without further purification. Double-distilled water was used during all of the experimental processes. A stoichiometric amount of $Ni(CH_3COO)_2.4H_2O$ and $Co(CH_3COO)_2.4H_2O$ was dissolved in 35 mL of ethylene glycol solution, referred to as solution A. The mixture was stirred for half an hour at 80 ℃ on a hot plate. In 5 mL of cold dilute HNO_3, the stoichiometrically calculated amount of TIP was added and stirred to get a clear solution followed by adding it to the above solution A. Then the reaction was continued for 6 h with stirring at 80 ℃. The sample mixture was initially heated at 400 ℃ for 1 h. Finally, different colors of undoped and doped $NiTiO_3$ samples were obtained by heating the samples in a sintering muffle furnace at 800 ℃ for 3 hrs with an intermediate grinding step to get single-phase material with a heating rate of 5 ℃/min in air. The series of $Ni_{1-x}Co_xTiO_3$ samples were denoted as NCTO-0, NCTO-5, NCTO-10, NCTO-15, NCTO-17.5, NCTO-20, and NCTO-25 for (x = 0.05, 0.1, 0.15, 0.175, 0.2, 0.25), respectively, in this manuscript.

4.3 Result and Discussion

4.3.1 XRD Studies Rietveld Refinement

The well-separated diffraction peaks of the $Ni_{1-x}Co_xTiO_3$ (x = 0.05, 0.1, 0.15, 0.175, 0.2, 0.25) samples in the XRD pattern **Figure 4.1a** confirms the presence of ilmenite $NiTiO_3$ with a rhombohedral phase R-3 (148) space group, is indicative of the material's crystalline form and are well-indexed with the $NiTiO_3$ (JCPDS No. 33-0960). The X-ray diffraction spectrum is also utilized to estimate the average crystallite size "D" of $Ni_{1-x}Co_xTiO_3$ (x = 0 - 0.25) samples using the Debye-Scherrer formula as follows:

$$D = 0.9\lambda/\beta cos\theta \qquad (4.2)$$

where *D* is crystallite size, λ is the wavelength of the X-ray radiation (1.54 Å for Cu Kα), β is the full-width half maxima and θ is the diffraction angle, was used to calculate crystallite size. [27] The average crystallite size was found to increase from ~41.1 (±1) to ~49.3 (±1) nm with increasing doping percentage of Co, this is due to larger ionic radii of dopant ion Co^{2+} (0.72 Å) compared to Ni^{2+} ions (0.69 Å). Further, Rietveld refinement of NCTO samples was performed by taking Pseudo-Voigt as peak profile function, rhombohedral phase, and R-3 (148) space group, shown in **Figure 4.1 (b, c)**. The refinement results along with their reliability factors (R_{wp}, and χ^2) were listed in **Table 4.1**. It is clear from the refinement that the lattice parameter slightly increases in comparison with the pure $NiTiO_3$ because of the larger ionic radius of Co^{2+} than Ni^{2+}. To evaluate how the introduction of Co influences the stability of the crystal structure, we computed the Goldschmidt tolerance (t) factor. The Goldschmidt tolerance (t) factor for an ABO_3-type ilmenite structure is defined as: [28, 29]

$$t = \frac{1}{3}\left(\frac{(\sqrt{2}+1)R_O^{-2}+R_B)}{R_O^{-2}+x\,R'_A+(1-x)R_A} + \frac{\sqrt{2}R_O^{-2}}{R_O^{-2}+R_B}\right) \quad (4.3)$$

where R_A, R'_A, R_B, and R_O^{2-} are the ionic radii of A [Ni^{2+} (0.69 Å)], A' [Co^{2+} (0.72 Å)], B [Ti^{4+} (0.60 Å)] and [O^{2-} (1.4Å)], respectively.[30]

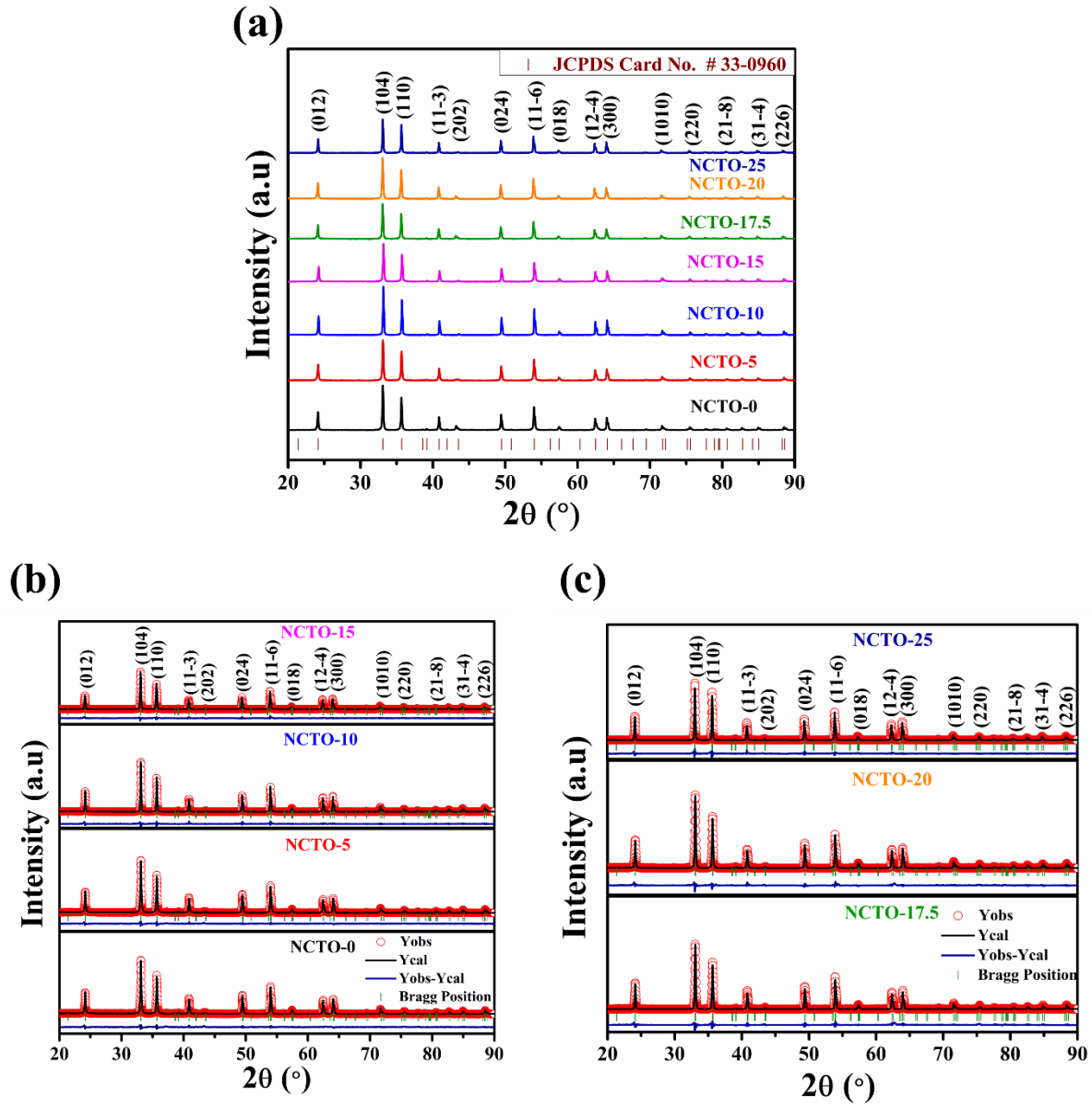

Figure. 4.1 (a) XRD pattern of all sol-gel synthesized NCTO samples **(b)**, **(c)** Rietveld refined XRD profile of $Ni_{1-x}Co_xTiO_3$ (x = 0.05, 0.1, 0.15, 0.175, 0.2, 0.25).

Based on this, substituting Ni^{2+} with these larger ions would slightly decrease the tolerance factor as x increases (**Table 4.1**), but it would remain within the range of 1 > t > 0.745. The tolerance factor (t) for $Ni_{1-x}Co_xTiO_3$ (*x* = 0.05, 0.1, 0.15, 0.175, 0.2, and 0.25) respectively are 0.9556, 0.9553, 0.9551, 0.9548, 0.9546, 0.9545 and 0.9542.

Table 4.1: The obtained lattice parameters and tolerance factor of $NiTiO_3$ and Co-doped $NiTiO_3$ samples are as follows:

Samples	Lattice parameter (Å)		Unit cell Volume, $(Å)^3$	R_{wp}	χ^2	Tolerance factor (t)
	a = b	c				
NCTO-0	5.0311	13.7981	302.45	9.36	2.41	0.9556
NCTO-5	5.0315	13.7992	302.50	9.89	2.45	0.9553
NCTO-10	5.0348	13.8074	303.10	9.87	2.17	0.9551
NCTO-15	5.0360	13.8131	303.37	9.45	2.87	0.9548
NCTO-17.5	5.0370	13.8176	303.59	10.76	2.92	0.9546
NCTO-20	5.0376	13.8190	303.69	10.89	3.01	0.9545
NCTO-25	5.0408	13.8218	304.36	12.45	3.13	0.9542

4.3.2 FT-IR Analysis

The bonding interactions in the synthesized NCTO powder samples were investigated by recording FT-IR spectra in the region 400–4000 cm^{-1}. The bands in the FT-IR spectra are marked as a, b, c, d, and e. The characteristic vibrational bands of metal-oxygen bonds are observed in the range of 400–700 cm^{-1} in the FT-IR spectrum of NCTO samples as shown in **Figure. 4.2**. The strong bands that appeared at 547 (b) and 717 (c) cm^{-1} are mainly due to the stretching vibration modes of Ni–O and Ti–O bonds. The sharp absorption band at 449 (a) cm^{-1} confirms the formation of Ni–O-Ti bonds. The weak absorption band (e) at 3440 cm^{-1} corresponds to the stretching vibration mode of hydroxyl (–OH) groups. The other vibrational bands observed at 1640 cm^{-1} (d) are mainly due to the bending modes of Ti–OH bonds. [31-33]

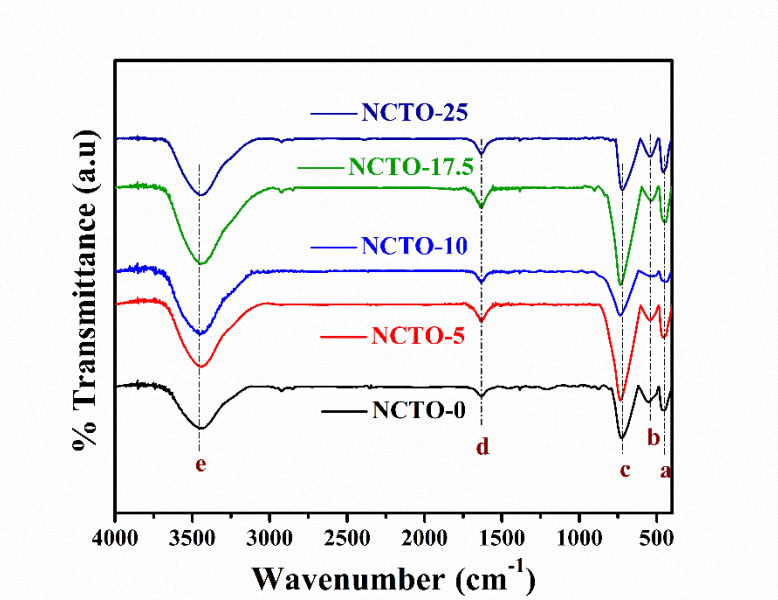

Figure. 4.2: FTIR spectra of NCTO-(0, 5, 10, 17.5, 25) samples.

4.3.3 XPS Studies

XPS experiments were carried out to confirm the valence state of the elements (Ni, Ti, and Co) in NCTO-0 and NCTO-17.5 samples. The XPS spectrum **Figure. 4.3 (a, b)** were deconvoluted using the Voigt peak function and the linear background with the XPS Peak41 program to precisely determine the double peak characteristics of Ni ($2p_{1/2}$) and Ni ($2p_{3/2}$). The Ni $2p$ signals at 855.4 and 873.2 eV are attributed to $2p_{3/2}$ and $2p_{1/2}$ of Ni^{2+}, and the additional peaks located at around 861.0 and 879.3 eV are matched to their respective satellite peaks.[34, 35] Further, the Ni $2p_{3/2}$ peak was found to be shifted by around 0.2 eV from 855.4 to 855.6 eV in the NCTO-17.5 sample compared to the NCTO-0 sample (no Co-doped sample). This shift confirms the doping of more electronegative ions into the lattice, there is the presence of a certain proportion of Co^{3+} in addition to Co^{2+}, where the more electronegative Co^{3+} ions incorporated into the lattice increase the ionicity of the Ni−O bond through the inductive effect. The deconvoluted Co $2p$ spectra of NCTO-17.5 (shown in **Figure. 4.3 c)** have $2p_{3/2}$ and $2p_{1/2}$ peaks marked at 781.2 and 796.6 eV, respectively, belong to Co^{2+} ions and the $2p_{3/2}$ and $2p_{1/2}$ peaks marked at 779.8 and 795.4 eV, respectively, belong

to Co^{3+} ions. In addition, there are two satellite peaks at 785.8 eV and 802.1 eV indicating that the most of Co element in the NCTO- 17.5 is a Co^{2+} cation. [36] The observed fractional composition of Co^{2+}: Co^{3+} in NCTO-17.5 was 0.88:0.12. The Ti 2*p* core-level spectra of NCTO-0 and NCTO-17.5 as shown in **Figure. 4.3 d**, **e** respectively, exhibit two peaks centered at 464.1 and 458.5 eV.

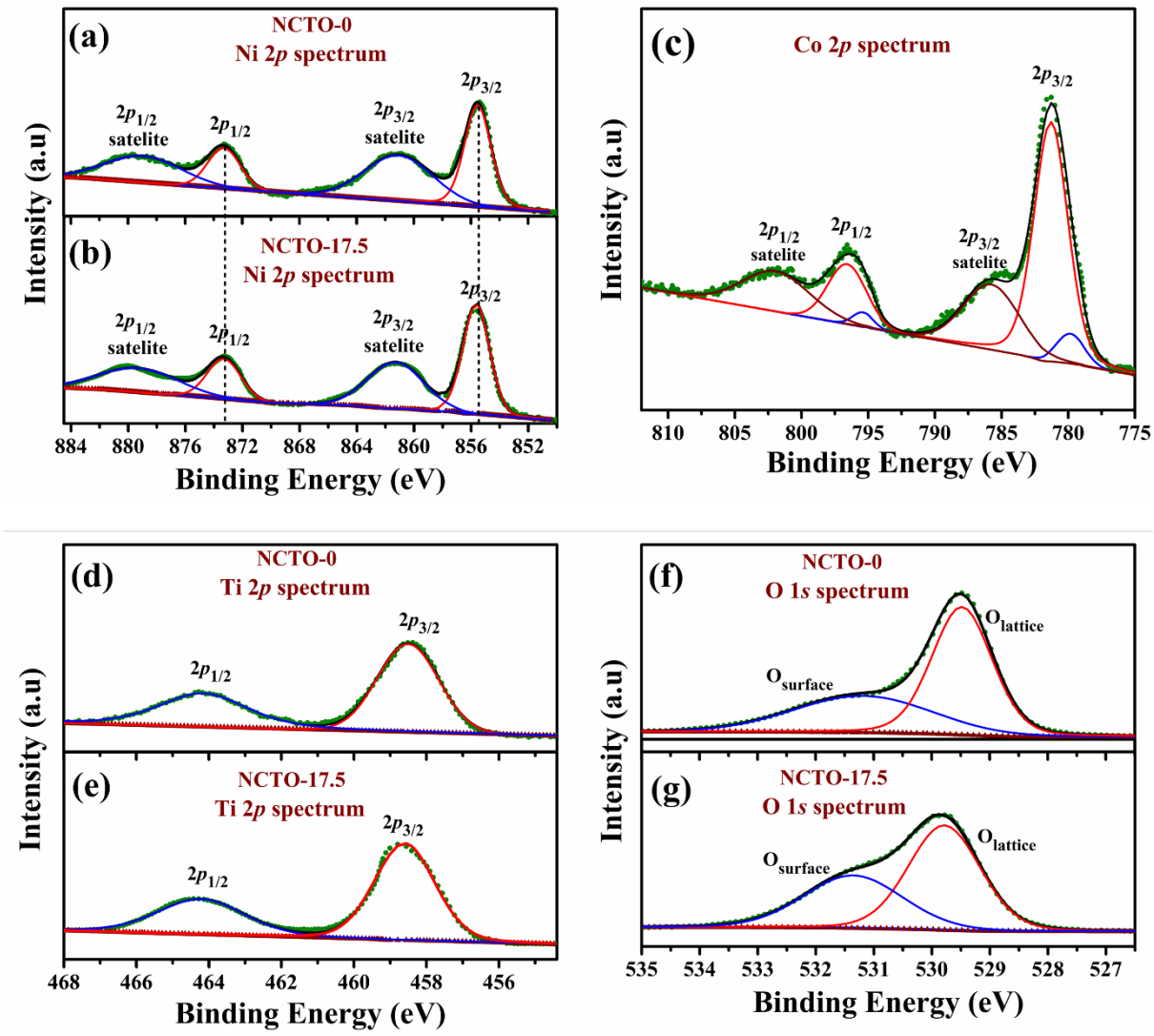

Figure. 4.3: Core level XPS spectrum of **(a), (b)** Ni (2*p*), **(c)**, Co (2*p*), **(d), (e)** Ti (2*p*) **(f), (g)** O (1*s*).

These peaks correspond to Ti ($2p_{1/2}$) and Ti ($2p_{3/2}$) respectively, confirming that Ti is present in the +4-oxidation state.[37, 38] The O 1*s* spectrum of NCTO-0, and NCTO-17.5 (**Figure.**

4.3 f, **g**) respectively, was deconvoluted into two peaks. The peaks at 529.5 and 531.1 eV correspond to lattice oxygen and surface hydroxyl oxygen respectively. [39]

4.3.4 Microstructural Analysis

The surface morphology and particle size distribution of the as-synthesized NCTO-0 and NCTO-17.5 samples were studied from the scanning electron micrographs. The SEM image of the NCTO-0 and NCTO-17.5 samples is shown in **Figure. 4.4 (a, b)** depicts the uniform and homogeneous agglomerated particles, distributed in the entire region of the micrograph.

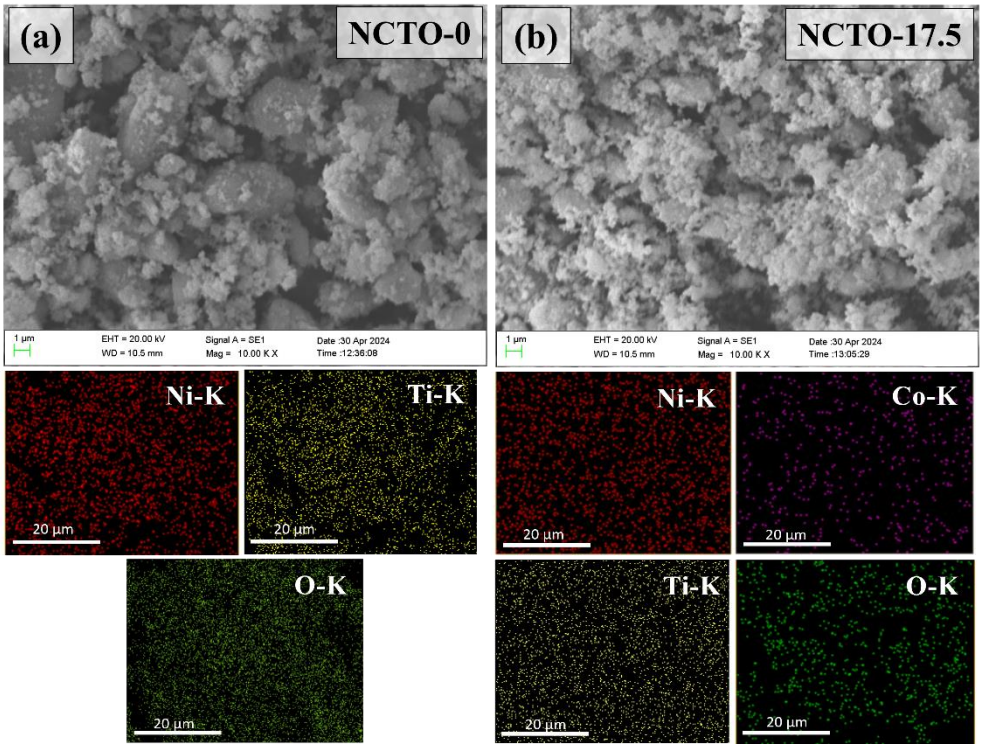

Figure. 4.4: SEM micrograph of **(a)** NCTO-0 (the scale bars are 1 µm), bottom two left panels represent elemental mapping of individual elements (Ni, Ti, and O) present in the NCTO-0 and **(b)** NCTO-17.5 (the scale bars are 1 µm), bottom two right panels represent elemental mapping of individual elements (Ni, Co, Ti, and O) present in the NCTO-17.5 sample.

The elemental color mapping of the NCTO-0 and NCTO-17.5 samples are shown in the bottom panels of **Figure. 4.4 a** and **Figure. 4.4 b** respectively, confirms the homogeneous

distribution of the element in the samples. The microstructure of the synthesized NCTO-17.5 was further confirmed with the bright-field TEM image of the sample (in **Figure. 4.5 a, b**) indicating highly crystalline quasi-hexagonal particles existing in the synthesized material. The polyhedral shape of the particle was further confirmed through TEM analysis. The length of the faces and diameter of the polyhedral-shaped particle are measured using ImageJ software as given in **Figure. 4.5 b**.

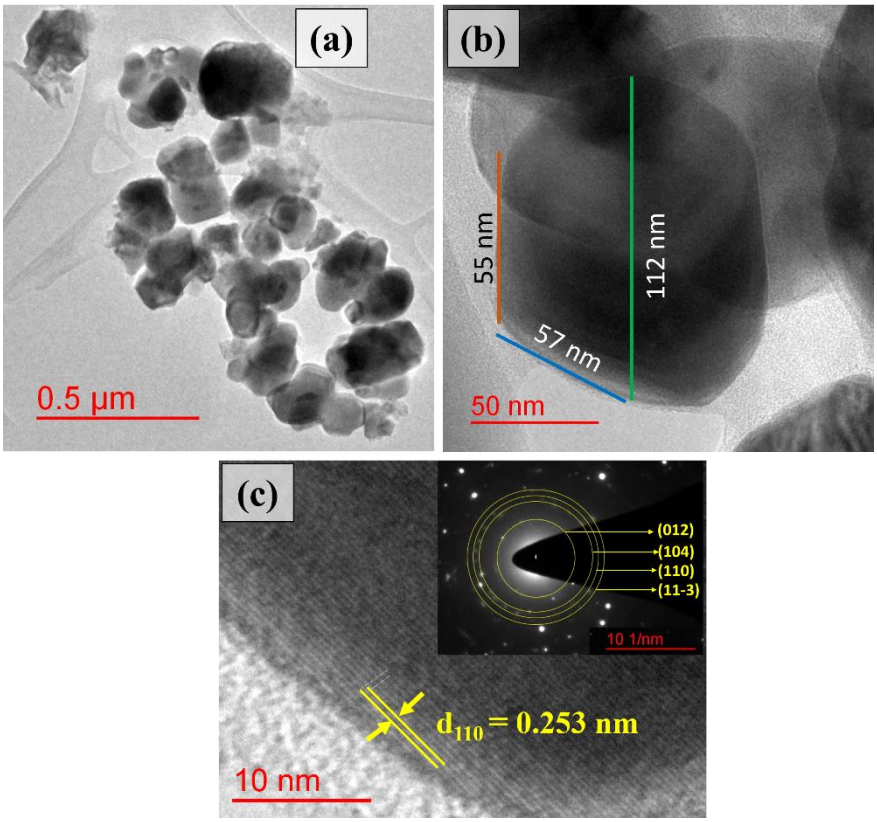

Figure. 4.5: Bright-field TEM images **(a), (b)** NCTO-17.5, and **(c)** HR-TEM image with interplanar d-spacing of (110) plane for NTO-17.5; inset shows the SAED pattern.

It shows that the length of the side faces are approximately in the range of 50–60 nm and and the diameter of the particle is approximately 112 nm. The lattice fringes of the NCTO-17.5 samples shown in **Figure 4.5 c**, correspond to the (110) plane and are in accordance with the XRD. The interplanar distances measured from the selected area electron diffraction (SAED) pattern show good agreement with the rhombohedral $NiTiO_3$. The diffraction rings are

indexed to (012), (104), (110), and (11-3) from the inside to the outside match well with the XRD results.

4.3.5 Electrochemical Studies

4.3.5.1 OER Performances of Synthesized Catalysts

The electrochemical performance of $Ni_{1-x}Co_xTiO_3$ ($0 \leq x \leq 0.25$) catalysts toward the OER was investigated in O_2-saturated 1 M KOH at a scan rate of 5 mVs^{-1} using a three-electrode setup. Before collecting the data in the range of 1.2 to 1.8 V *vs* RHE, several cycles of fast-scan cyclic voltammetry (CV) were conducted on the working electrode to achieve a stable current before collecting the data. The LSV curves are in **Figure. 4.6 a**, shows the OER performances of all the synthesized NCTO catalysts follow the order NCTO-0 < NCTO-5 < NCTO-10 < NCTO-25 < NCTO-20 < NCTO-15< NCTO-17.5. OER activity reaches its optimum performance for 17.5% Co doping and the activity decreases with further increase in the dopant concentration. Based on 10% solar water splitting conversion efficiency, the overpotential (η) needed to achieve a current density of 10 mA cm^{-2} is an important parameter in solar fuel synthesis. Consequently, it is important to compare the overpotential of the catalyst samples at this current density. [6] The overpotential in this context is defined as the difference between the observed OER potential at 10 $mAcm^{-2}$ and the theoretical reversible potential (1.23 V vs RHE). The overpotential needed to achieve a current density of 10 mA cm^{-2} for NCTO-s (s = 0 to 25) samples was determined to be 510, 482, 464, 416, 395, 428, and 445 mV respectively, as depicted in **Figure. 4.6 b.**

Tafel analysis stands as a fundamental study in the assessment of electrocatalysts for water electrolysis. The Tafel slope, illustrating the correlation between potential and the logarithm of current density, holds significance in evaluating reaction kinetics. [40]

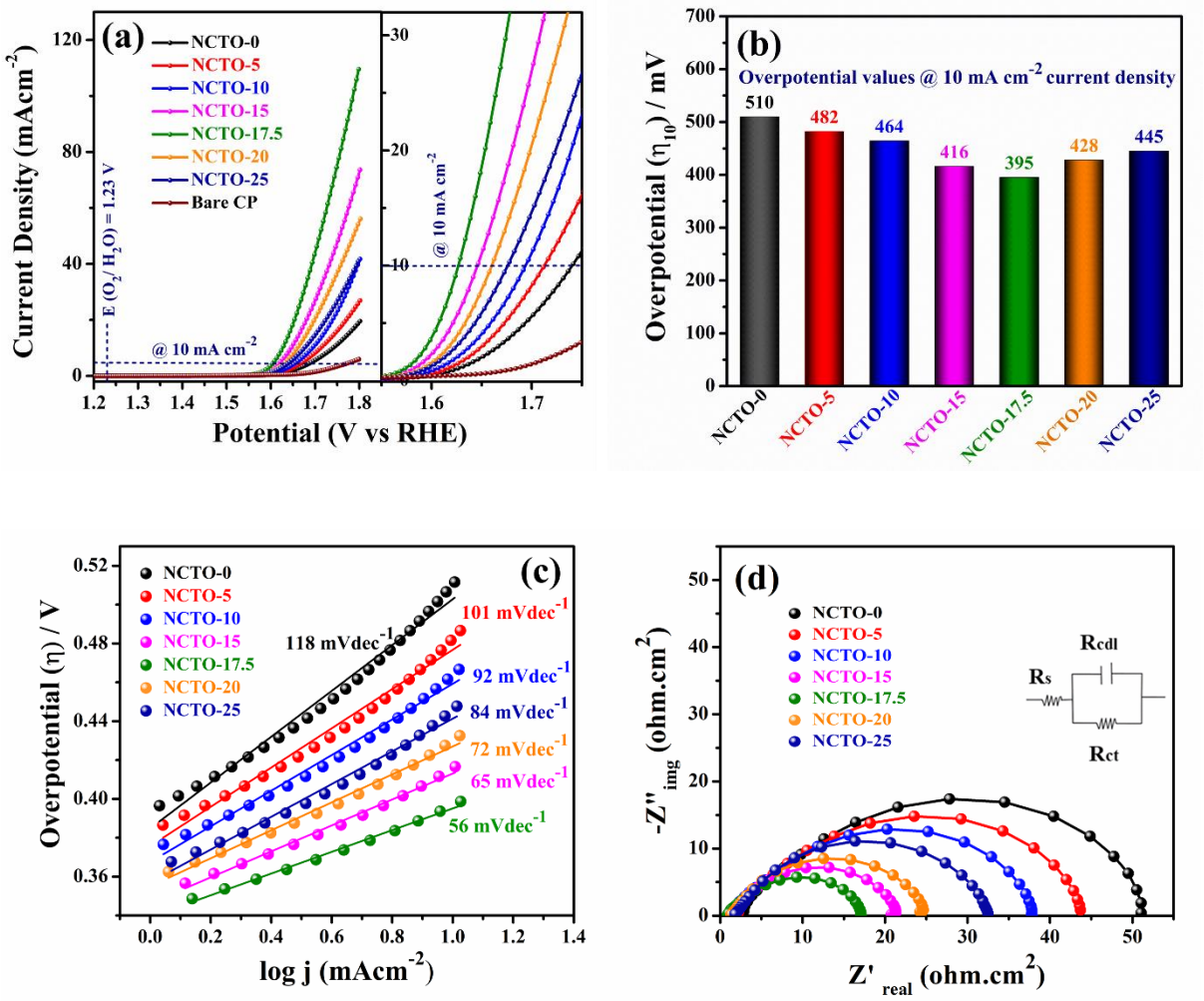

Figure. 4.6: OER performance of NCTO series samples $Ni_{1-x}Co_xTiO_3$ (x = 0.05, 0.1, 0.15, 0.175, 0.2, 0.25). **(a)** Linear sweep voltammograms taken at a scan rate of 5 mV s^{-1} in 1 M KOH, **(b)** Overpotentials at a current density of 10 mA cm^{-2}, **(c)** Tafel plots, **(d)** EIS recorded at 1.6 V vs. RHE.

Figure. 4.6 c shows the Tafel plot of a series of $Ni_{1-x}Co_xTiO_3$ ($0 \leq x \leq 0.25$) samples and the Tafel slope values obtained for NCTO-0, NCTO-5, NCTO-10, NCTO-15, NCTO-17.5, NCTO-20 and NCTO-25 are approximately 118, 101, 92, 65, 56, 72 and 84 mV dec^{-1}, respectively. A low Tafel slope value signifies a superior electrocatalyst with reduced overpotential. The lowest Tafel value observed for NCTO-17.5 (56 mV dec^{-1}) suggests its faster reaction kinetics compared to all other Co-doped $NiTiO_3$ catalysts. EIS measurements were performed and obtained the impedance spectra, analysis of these spectra allows for the determination of R_{ct}, among other parameters, providing insights into the electrochemical

performance and efficiency of the catalysts under investigation. Impedance studies for the catalysts $Ni_{1-x}Co_xTiO_3$ were conducted in the frequency range of 10 – 100 kHz with an AC amplitude of 10 mV at a potential of 1.6 V *vs* RHE, as shown in **Figure. 4.6 d**. Additionally, an equivalent circuit fit of the EIS data is in the inset of **Figure. 4.6 d**, shows the solution resistance (R*s*), charge-transfer resistance (R_{ct}) and double-layer capacitance (R_{Cdl}). The charge transfer resistance (R_{ct}) (diameter of the semicircle in the Nyquist plot at the high-frequency region) is linked with the electrochemical kinetics of the reaction. A smaller semicircle loop suggests lower charge-transfer resistance and a sign of faster kinetics during the OER process.[41] The R_{ct} value of NCTO-17.5 is found to be 16.13 Ω, which is lower than all other synthesized catalysts NCTO-0 (48.24 Ω), NCTO-5 (41.31 Ω), NCTO-10 (36.10 Ω), NCTO-15 (19.70 Ω), NCTO-20 (23.11 Ω) and NCTO-25 (30.31 Ω), indicating its faster OER kinetic rate compared to the other catalysts.

Moreover, the electrochemically active surface area (ECSA) of each catalyst was determined using double-layer capacitance measurement to investigate the intrinsic characteristics of the electrocatalyst. The double-layer capacitance (C_{dl}) is evaluated using cyclic voltammetry (CV) in a non-faradic potential range of 0.91 to 1.01 V. The scan rates used in the analysis vary from 40 to 140 mV/s, as depicted in **Figure. 4.7 (a-g)**. The change in current density (ΔJ) during anodic and cathodic sweeps in cyclic voltammetry (CV) is influenced by the charge-storage capacity of the working electrode and shows a linear increase as the scan rate increases. [42, 43]

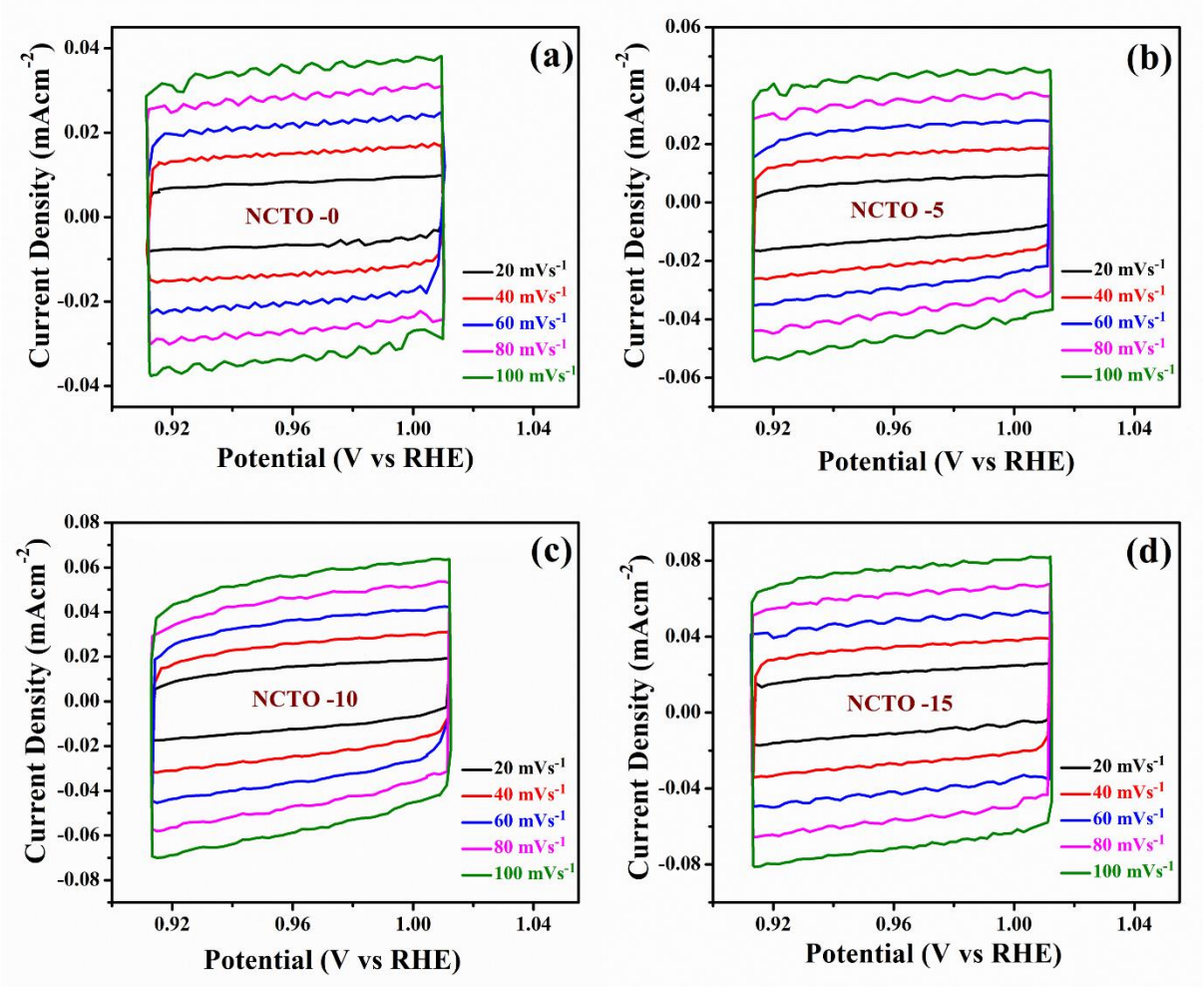
(a)
NCTO -0
(b)
NCTO -5
(c)
NCTO -10
(d)
NCTO -15
(e)
NCTO -17.5
(f)
NCTO -20
20 mVs-1
40 mVs-1
60 mVs-1
80 mVs-1
100 mVs-1
Current Density (mAcm-2)
Potential (V vs RHE)

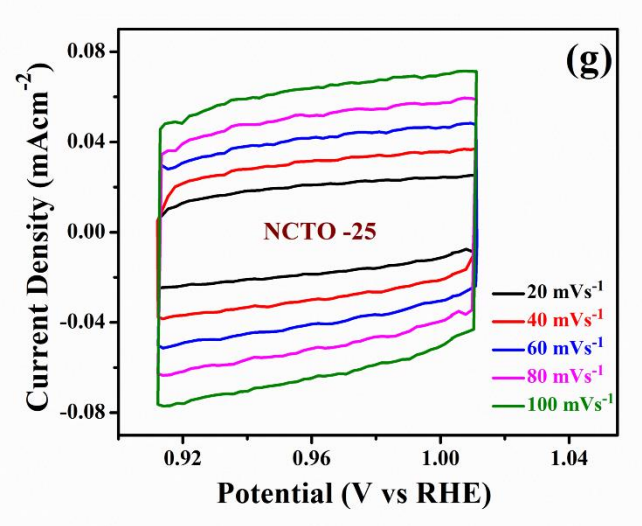

Figure. 4.7 Determination of double layer capacitance (C_{dl}) of NCTOs **(a-g)** CV measurements in a non-faradic current region (0.9-1.0 V vs. RHE) at scan rates of 20, 40, 60, 80 and 100 mV s^{-1} in 1 M KOH electrolyte.

The double-layer capacitance which is the slope of ΔJ/2 *vs* scan rate plot is found to be 0.36, 0.41, 0.53, 0.70, 0.76, 0.66, and 0.61 mF/cm^{-2} for all the NCTO series catalysts, which follows the order NCTO-0 < NCTO-5 < NCTO-10 < NCTO-25 < NCTO-20 < NCTO-15< NCTO-17.5 as plotted (**Figure. 4.7 a**) for each catalyst. The best electrocatalytic OER activity was obtained for NTO-17.5 or up to 17.5% Co doping in $NiTiO_3$ and OER activity decreases with further increase in Co doping at the Ni site in $NiTiO_3$ ilmenite structure.

The electrochemical active surface area (ECSA) of a catalyst is calculated using the double-layer capacitance with the formula: $ECSA = {}^{C_{dl}}/_{C_s}$ (4.3)

In this equation, C_{dl} represents the double-layer capacitance of the catalyst, while C_s denotes the specific capacitance of the material per unit area under identical electrolyte conditions, which is established as 0.04 mF cm^{-2} in a 1.0 M KOH solution. [44] The relationship between ECSA and the catalyst is depicted in **Figure. 4.7 b**, where it is evident that ECSA is highest for NCTO-17.5, after which no further increase in ECSA is observed.

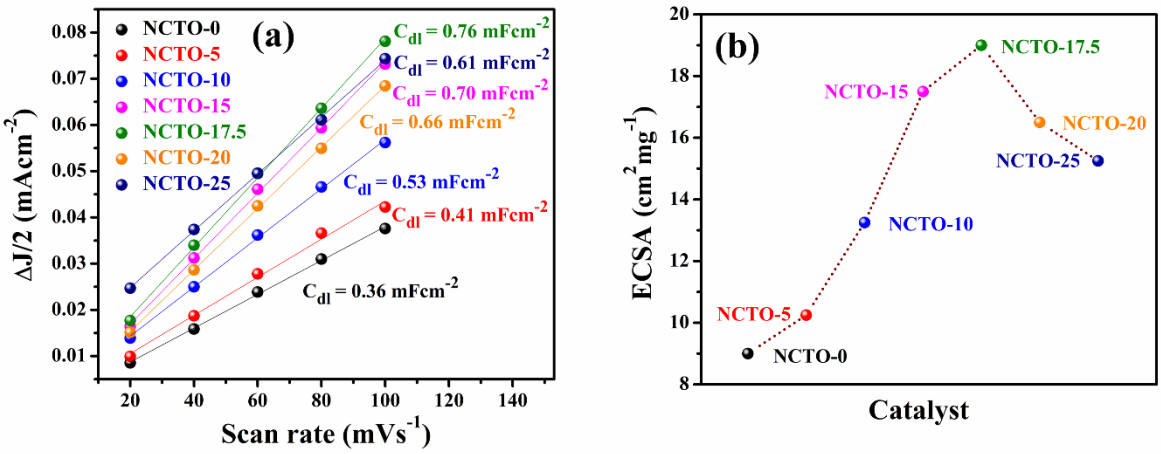

Figure. 4.8 (a) Plots of capacitive current density differences ΔJ/2 vs. the scan rate for all NCTO samples & **(b)** Plot of ECSA vs catalyst $Ni_{1-x}Co_xTiO_3$ (x = 0.05 - 0.25).

Table 4.2 The C_{dl} and corresponding ECSA values of all the catalysts

S. No.	Catalyst	C_{dl} (mF cm^{-2})	ECSA (cm^2 mg^{-1})
1	NCTO-0	0.36	9
2	NCTO-5	0.41	10.25
3	NCTO-10	0.53	13.25
4	NCTO-15	0.70	17.5
5	NCTO-17.5	0.76	19
6	NCTO-20	0.66	16.5
7	NCTO-25	0.61	15.25

The values of C_{dl} and the corresponding ECSA for all catalysts examined in this study are detailed in **Table 4.2**.

4.3.5.2 Long-term Stability Test

The stability of electrocatalysts is a critical factor for large-scale water electrolysis applications. [45] The static stability of NCTO-17.5 was evaluated through a chronoamperometric (CA) test conducted at 1.62 V vs RHE for 24 hours, as shown in **Figure. 4.9**, which shows that NCTO-17.5 exhibits a stable current density at a fixed applied potential with a current retention of ~94 % at 1.62 V operating voltage *vs.* RHE. The stability

of the NCTO-17.5 catalyst was evaluated through an accelerated degradation test (ADT) using fast-scan cyclic voltammetry (CV) cycling in a potentiodynamic mode.

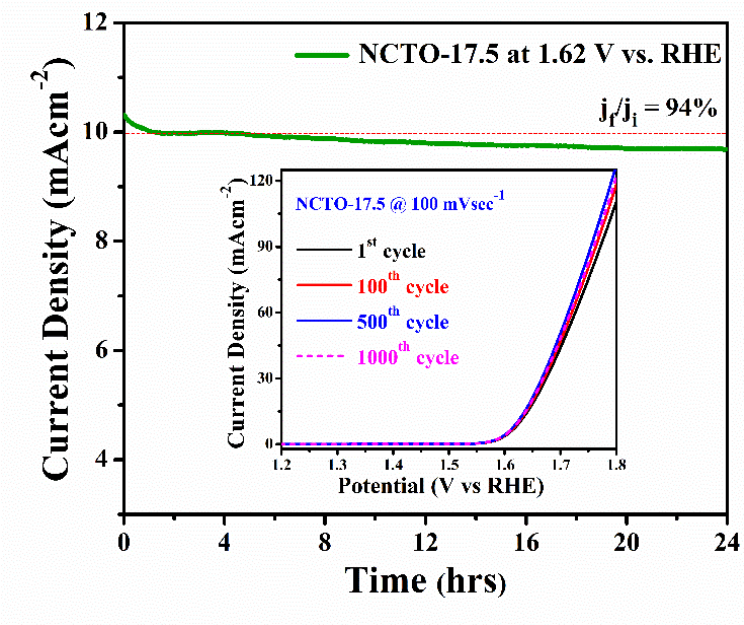

Figure.4.9: Chronoamperogram of NCTO-17.5 at an applied potential of 1.62 V *vs*. RHE for 24 hrs; inset shows the linear sweep voltammograms for the 1st, 100th, 500th, and 1000th cycle at a scan rate of 100 mV s^{-1}.

The test involved scanning 1000 CV cycles at a scan rate of 100 mV/s within a potential range of 1.2 to 1.8 V vs RHE. The inset of **Figure. 4.9** shows the linear sweep voltammetry (LSV) plots for the 1st, 100th, 500th, and 1,000th cycles. The results indicate only a marginal change in the overpotential at 10 mA cm^{-2} over the course of the 1000 cycles. This suggests that the NCTO-17.5 catalyst exhibits excellent stability under the highly alkaline conditions of the 1 M KOH electrolyte.

4.3.5.3 Post OER Characterization

The stability of the electrocatalyst NCTO-17.5 after extended electrochemical cycling was further verified through a post-characterization technique, i.e. post X-ray diffraction (XRD). The XRD analysis conducted on the NCTO-17.5 electrode after electrochemical testing revealed no changes in the diffraction pattern, except for a peak attributed to the carbon paper substrate. This indicates that the structural retention of the NCTO-17.5 catalyst is maintained after long-term electrochemical testing. The diffraction pattern aligns with the rhombohedral

phase R-3 (148) $NiTiO_3$, indexed well using the (JCPDS no. 33-0960) as illustrated in **Figure 4.10**.

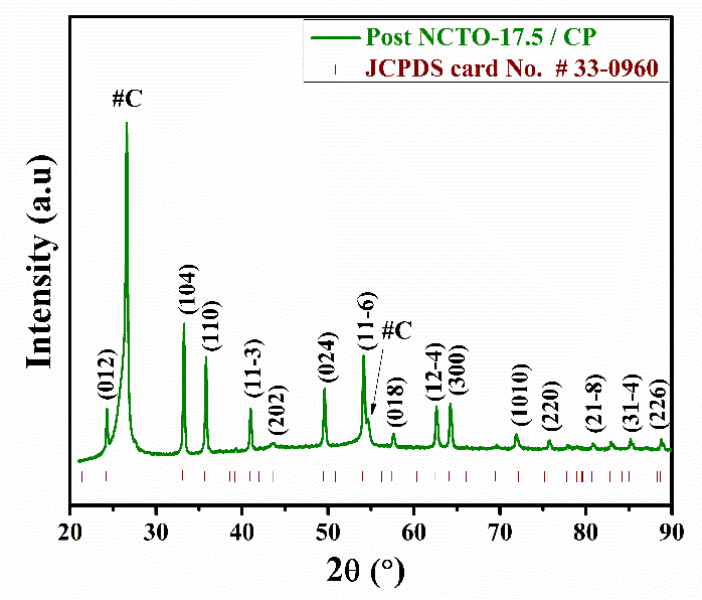

Figure 4.10. Post-OER XRD pattern of NCTO-17.5 electrode.

4.4. Conclusion

In summary, a series of ilmenite type Co-doped $NiTiO_3$ ($Ni_{1-x}Co_xTiO_3$, $0 < x < 0.25$) have been synthesized by the sol–gel route and investigated for the influence of Co doping on electrocatalytic activity toward the oxygen evolution reaction. 17.5% Co-doped $NiTiO_3$ is found to be the best OER catalyst in the series of $Ni_{1-x}Co_xTiO_3$($0 < x < 0.25$). The observed higher activity of Co-doped $NiTiO_3$ is due to the inductive effect generated by Co substitution on Ni site in ilmenite $NiTiO_3$ structure. $Ni^{2+/3+}$ is the active site for OER as Ni(3*d*) orbital are pinned over O(2*p*) orbitals. The Co^{3+} enhances the ionicity of the Ni–O bond in the lattice through the inductive effect (supported by XPS; **Figure. 4.3a**). XPS study confirms the high electro-positivity of Ni ions. The higher ionicity of Ni–O leads to a greater overlap between Ni(3*d*) and O(2*p*) orbital resulting in a higher catalytic activity of the doped catalysts. An increase in the Co concentration beyond an optimum level leads to decrease in the OER activity of the catalyst as with higher substitution of Co on the Ni site, concentration of

catalytic active centers ($Ni^{2+/3+)}$ decreases in the catalyst. An optimum concentration of 17.5% Co doping leads to the best activity via its inductive effect on the redox potential of the active species, namely Ni^{2+}/Ni^{3+} parent species. Also, this optimum concentration of 17.5% Co in $NiTiO_3$ shows the best OER activity and $Ni_{0.825}Co_{17.5}TiO_3$ depicts a Tafel slope of 56 mV dec^{-1} and an overpotential of 395 mV at a current density of 10 mA cm^{-2}.

4.5. References

1. Turner, J. A. Sustainable Hydrogen Production. *Science* **2004**, *305*, 972–974.
2. Gupta, A.; Kushwaha, V.; Mondal, R.; Singh, A. N.; Prakash, R.; Mandal, K. D.; Singh, P. $SrFeO_{3-\delta}$: A Novel $Fe^{4+} \leftrightarrow Fe^{2+}$ Redox Mediated Pseudocapacitive Electrode in Aqueous Electrolyte. *Physical Chemistry Chemical Physics* **2022**, *24*, 11066–11078.
3. Kumar, S.; Ranjeeth, R.; Mishra, N. K.; Prakash, R.; Singh, P. NASICON-Structured $Na_3Fe_2PO_4(SO_4)_2$: A Potential Cathode Material for Rechargeable Sodium-Ion Batteries. *Dalton Transactions* **2022**, *51*, 5834–5840.
4. Soni, V.; Singh, A. N.; Singh, P.; Gupta, A. Photocatalytic Dye-Degradation Activity of Nano-Crystalline $Ti_{1-x}M_xO_{2-\delta}$ (M =Ag, Pd, Fe, Ni and x = 0, 0.01) for Water Pollution Abatement. *RSC Adv* **2022**, *12*, 18794–18805.
5. Soni, V.; Jaiswal, S.; Nigam, K. G.; Singh, P.; Gupta, A. Nickel-Doped Lithium-Vacant Layered $Li_yCr_{1-x}Ni_xO_2$: A Potentially Active Electrocatalyst for the Oxygen Evolution Reaction. *J. Mater. Chem. A* **2024**, *12*, 19212–19226.
6. Soni, V.; Jaiswal, S.; Singh, P.; Gupta, A. Aluminum-Doped Lithium-Vacant Layered $Li_{1-x}Cr_{1-x}Al_xO_2$: A Potentially Active Electrocatalyst for the Oxygen Evolution Reaction. *ACS Appl. Energy Mater.* **2024**, *7*, 3175–3186.
7. Mondal, R.; Ratnawat, H.; Mukherjee, S.; Gupta, A.; Singh, P. Investigation of the Role of Sr and Development of Superior Sr-Doped Hexagonal $BaCoO_{3-\delta}$ Perovskite Bifunctional OER/ORR Catalysts in Alkaline Media. *Energy & Fuels* **2022**, *36*, 3219–3228.
8. Han, N.; Zhang, W.; Guo, W.; Pan, H.; Jiang, B.; Xing, L.; Tian, H.; Wang, G.; Zhang, X.; Fransaer, J. Designing Oxide Catalysts for Oxygen Electrocatalysis: Insights from Mechanism to Application. *Nanomicro Lett.* **2023**, *15*, 185.
9. Thippani, T.; Mandal, S.; Wang, G.; Ramani, V. K.; Kothandaraman, R. Probing Oxygen Reduction and Oxygen Evolution Reactions on Bifunctional Non-Precious Metal Catalysts for Metal–Air Batteries. *RSC Adv.* **2016**, *6*, 71122–71133.
10. Liu, D.; Zhao, Z.; Xu, Z.; Li, L.; Lin, S. Anchoring Ce-Modified $Ni(OH)_2$ Nanoparticles on Ni-MOF Nanosheets to Enhances the Oxygen Evolution Performance. *Dalton Transactions* **2022**, *51*, 12839–12847.
11. Gong, M.; Dai, H. A Mini Review of NiFe-Based Materials as Highly Active Oxygen Evolution Reaction Electrocatalysts. *Nano Res.* **2015**, *8*, 23–39.
12. Moschkowitsch, W.; Dhaka, K.; Gonen, S.; Attias, R.; Tsur, Y.; Caspary Toroker, M.; Elbaz, L. Ternary NiFeTiOOH Catalyst for the Oxygen Evolution Reaction: Study of the Effect of the Addition of Ti at Different Loadings. *ACS Catal.* **2020**, *10*, 4879–4887.
13. Mondal, R.; Ratnawat, H.; Kumar, S.; Kumar, A.; Singh, P. Ni Stabilized Rock-Salt Structured CoO; $Co_{1-x}Ni_xO$: Tuning of e_g Electrons to Develop a Novel OER Catalyst. *RSC Adv.* **2020**, *10*, 17845–17853.
14. Brehm, J. A.; Bennett, J. W.; Schoenberg, M. R.; Grinberg, I.; Rappe, A. M. The Structural Diversity of ABS_3 Compounds with *d* Electronic Configuration for the *B* -Cation. *J Chem Phys.* **2014**, *140*.

15. Lettieri, S.; Pavone, M.; Fioravanti, A.; Santamaria Amato, L.; Maddalena, P. Charge Carrier Processes and Optical Properties in TiO_2 and TiO_2-Based Heterojunction Photocatalysts: A Review. *Materials* **2021**, *14*, 1645.
16. Bockris, J. O.; Otagawa, T. The Electrocatalysis of Oxygen Evolution on Perovskites. *J Electrochem Soc.* **1984**, *131*, 290–302.
17. Suen, N.-T.; Hung, S.-F.; Quan, Q.; Zhang, N.; Xu, Y.-J.; Chen, H. M. Electrocatalysis for the Oxygen Evolution Reaction: Recent Development and Future Perspectives. *Chem Soc Rev.* **2017**, *46*, 337–365.
18. Lambert, T. N.; Vigil, J. A.; White, S. E.; Davis, D. J.; Limmer, S. J.; Burton, P. D.; Coker, E. N.; Beechem, T. E.; Brumbach, M. T. Electrodeposited $Ni_xCo_{3-x}O_4$ Nanostructured Films as Bifunctional Oxygen Electrocatalysts. *Chem. Comm.* **2015**, *51*, 9511–9514.
19. Wu, G.; Li, N.; Zhou, D.-R.; Mitsuo, K.; Xu, B.-Q. Anodically Electrodeposited Co+Ni Mixed Oxide Electrode: Preparation and Electrocatalytic Activity for Oxygen Evolution in Alkaline Media. *J Solid State Chem.* **2004**, *177*, 3682–3692.
20. Yan, X.; Li, K.; Lyu, L.; Song, F.; He, J.; Niu, D.; Liu, L.; Hu, X.; Chen, X. From Water Oxidation to Reduction: Transformation from $Ni_xCo_{3-x}O_4$ Nanowires to $NiCo/NiCoO_x$ Heterostructures. *ACS Appl Mater Interfaces* **2016**, *8* (5), 3208–3214.
21. Zhao, Y.; Jia, X.; Chen, G.; Shang, L.; Waterhouse, G. I. N.; Wu, L.-Z.; Tung, C.-H.; O'Hare, D.; Zhang, T. Ultrafine NiO Nanosheets Stabilized by TiO_2 from Monolayer NiTi-LDH Precursors: An Active Water Oxidation Electrocatalyst. *J Am Chem Soc.* **2016**, *138*, 6517–6524.
22. Yang, Y.; Kao, L. C.; Liu, Y.; Sun, K.; Yu, H.; Guo, J.; Liou, S. Y. H.; Hoffmann, M. R. Cobalt-Doped Black TiO_2 Nanotube Array as a Stable Anode for Oxygen Evolution and Electrochemical Wastewater Treatment. *ACS Catal.* **2018**, *8*, 4278–4287.
23. Sachin Kumar, B.; Tarafder, K.; Shetty, A. R.; Hegde, A. C.; Gudla, V. C.; Ambat, R.; Kalpathy, S. K.; Anandhan, S. Polymorph Nickel Titanate Nanofibers as Bifunctional Electrocatalysts towards Hydrogen and Oxygen Evolution Reactions. *Dalton Trans.* **2019**, *48*, 12684–12698.
24. Dong, C.; Liu, X.; Wang, X.; Yuan, X.; Xu, Z.; Dong, W.; Riaz, M. S.; Li, G.; Huang, F. Hierarchical $Ni/NiTiO_3$ Derived from NiTi LDHs: A Bifunctional Electrocatalyst for Overall Water Splitting. *J Mater Chem A* **2017**, *5*, 24767–24774.
25. Kuznetsov, D. A.; Han, B.; Yu, Y.; Rao, R. R.; Hwang, J.; Román-Leshkov, Y.; Shao-Horn, Y. Tuning Redox Transitions via Inductive Effect in Metal Oxides and Complexes, and Implications in Oxygen Electrocatalysis. *Joule* **2018**, *2*, 225–244.
26. Chen, H.; Fu, W.; Geng, Z.; Zeng, J.; Yang, B. Inductive Effect as a Universal Concept to Design Efficient Catalysts for CO_2 Electrochemical Reduction: Electronegativity Difference Makes a Difference. *J Mater Chem A* **2021**, *9*, 4626–4647.
27. Kushwaha, V.; Gupta, A.; Choudhary, R. B.; Mandal, K. D.; Mondal, R.; Singh, P. Nanocrystalline β-NiS: A Redox-Mediated Electrode in Aqueous Electrolyte for Pseudocapacitor/Supercapacitor Applications. *Phys Chem Chem Phys.* **2023**, *25*, 555–569.

28. Tursun, R.; Su, Y. C.; Yu, Q. S.; Tan, J.; Hu, T.; Luo, Z. B.; Zhang, J. Effect of Doping on the Structural, Magnetic, and Ferroelectric Properties of $Ni_{1-X}A_xTiO_3$ (A = Mn, Fe, Co, Cu, Zn; X = 0, 0.05, and 0.1). *J Alloys Compd.* **2019**, *773*, 288–298.
29. Liu, X.; Hong, R.; Tian, C. Tolerance Factor and the Stability Discussion of ABO_3-Type Ilmenite. *J. Mater. Sci: Mater Electron.* **2009**, *20*, 323–327.
30. Shannon, R. D.; Prewitt, C. T. Effective Ionic Radii in Oxides and Fluorides. *Acta Crystallogr B* **1969**, *25*, 925–946.
31. Pavithra, C.; Madhuri, W. Electrical and Magnetic Properties of $NiTiO_3$ Nanoparticles Synthesized by the Sol-Gel Synthesis Method and Microwave Sintering. *Mater Chem Phys.* **2018**, *211*, 144–149.
32. Gaddimath, S.; Chandrakala, K. B.; Lagashetty, A.; Dani, S.; Prabhu, C. P. K.; Giddaerappa; Sannegowda, L. K. Ilmenite-Type $NiTiO_3$ Nanoparticles for Oxygen Evolution Reaction. *J Appl Electrochem* **2024**, *54*, 2519–2536.
33. Souri, A. P.; Andrigiannaki, N.; Moschogiannaki, M.; Faka, V.; Kiriakidis, G.; Malankowska, A.; Zaleska-Medynska, A.; Binas, V. Metal Titanate ($ATiO_3$, A: Ni, Co, Mg, Zn) Nanorods for Toluene Photooxidation under LED Illumination. *Applied Sciences* **2021**, *11*, 10850.
34. Lakshmi, T.; Hajarabeevi, N.; Mishra, T.; Aman, N. Synthesis of Cobalt Doped Nickel Titanate Nanomaterials for Enhanced Photocatalytic Reduction of Chromium. *Optik* **2024**, *298*, 171561.
35. Sahoo, S.; Satpati, A. K.; Sahoo, P. K.; Naik, P. D. Incorporation of Carbon Quantum Dots for Improvement of Supercapacitor Performance of Nickel Sulfide. *ACS Omega* **2018**, *3*, 17936–17946.
36. Huang, J.; Qian, W.; Ma, H.; Zhang, H.; Ying, W. Highly Selective Production of Heavy Hydrocarbons over Cobalt–Graphene–Silica Nanocomposite Catalysts. *RSC Adv.* **2017**, *7*, 33441–33449.
37. Jaiswal, S.; Mondal, R.; Kushwaha, V.; Gupta, A.; Singh, P. Tuning of Redox Energy of Transition-Metal Ions through the Utilization of Interlayer Potentials in Layered Perovskites: Development of a Titanium-Based Superior HER Catalyst in an Acidic Medium. *ACS Appl Energy Mater* **2023**, *6*, 7323–7334.
38. Xie, W.; Li, R.; Xu, Q. Enhanced Photocatalytic Activity of Se-Doped TiO_2 under Visible Light Irradiation. *Sci Rep.* **2018**, *8*, 8752.
39. Gupta, A.; Kushwaha, V.; Mondal, R.; Singh, A. N.; Prakash, R.; Mandal, K. D.; Singh, P. $SrFeO_{3-\delta}$: A Novel $Fe^{4+} \leftrightarrow Fe^{2+}$ Redox Mediated Pseudocapacitive Electrode in Aqueous Electrolyte. *Phy Chem Chem Phy.* **2022**, *24*, 11066–11078.
40. Shinagawa, T.; Garcia-Esparza, A. T.; Takanabe, K. Insight on Tafel Slopes from a Microkinetic Analysis of Aqueous Electrocatalysis for Energy Conversion. *Sci Rep.* **2015**, *5*, 13801.
41. Soni, V.; Mondal, R.; Singh, A. N.; Singh, P.; Gupta, A. Dumbbell Defect Containing Chromium-Rich Lithium-Vacant Layered $Li_yCr_{1-x}Fe_xO_2$ ($y \leq 1$, $0 \leq x \leq 0.2$): An Unexplored and Highly Efficient Electrocatalyst for the Oxygen Evolution Reaction. *ACS Appl Energy Mater* **2023**, *6*, 1308–1320.

42. Liu, X.; Zhai, Z.-Y.; Chen, Z.; Zhang, L.-Z.; Zhao, X.-F.; Si, F.-Z.; Li, J.-H. Engineering Mesoporous NiO with Enriched Electrophilic Ni^{3+} and O^{-} toward Efficient Oxygen Evolution. *Catalysts* **2018**, *8*, 310.
43. Jaiswal, S.; Soni, V.; Singh, P.; Gupta, A. Role of Cation Deficiency and the Inductive Effect in Ti-Doped NiO for Developing Superior Electrocatalysts for the Oxygen Evolution Reaction. *ACS Appl Energy Mater.* **2024**, *7*, 8814–8825.
44. McCrory, C. C. L.; Jung, S.; Peters, J. C.; Jaramillo, T. F. Benchmarking Heterogeneous Electrocatalysts for the Oxygen Evolution Reaction. *J Am Chem Soc.* **2013**, *135*, 16977–16987.
45. Anantharaj, S.; Ede, S. R.; Sakthikumar, K.; Karthick, K.; Mishra, S.; Kundu, S. Recent Trends and Perspectives in Electrochemical Water Splitting with an Emphasis on Sulfide, Selenide, and Phosphide Catalysts of Fe, Co, and Ni: A Review. *ACS Catal.* **2016**, *6*, 8069–8097.